Materials Advances

ROYAL SOCIETY OF CHEMISTRY

PAPER

View Article Online
View Journal | View Issue

Check for updates

Cite this: *Mater. Adv.*, 2023, 4, 5263

Phosphorus and nitrogen co-doped reduced graphene oxide as superior electrode nanomaterials for supercapacitors†

Khaled Rhili,[a] Siham Chergui,[a] Juan Carlos Abergo-Martinez,[a] Ahmad Samih El Douhaibi[b] and Mohamed Siaj *[a]

Received 15th August 2023,
Accepted 9th September 2023

DOI: 10.1039/d3ma00553d

rsc.li/materials-advances

Phosphorus/nitrogen co-doped reduced graphene oxide (PN-rGO) materials have been prepared by one-step pyrolysis of the functionalized GO (FGO) with hexachlorocyclotriphosphazene and *p*-phenylenediamine. The resulting PN-rGO shows a porous structure with a transparent and wrinkled thin film morphology. Compared with undoped rGO, the electrochemical measurements of PN-rGO reveal enhanced capacitive properties, including a high specific capacitance of 292 F g^{-1} at 0.5 A g^{-1}, remarkable rate capability, and excellent cycling stability (after 10 000 cycles, 97% capacitance is maintained). Moreover, the assembled symmetric supercapacitor using PN-rGO shows a relatively high energy density of 8.2 W h kg^{-1} at a power density of 570 W kg^{-1} in KOH electrolyte. The outstanding performance of this material as a supercapacitor electrode may be attributed to the pseudocapacitive effect of P/N co-doping in reduced graphene nanosheets, as well as its exceptional porous structure.

1. Introduction

Recently, carbon-doped heteroatoms have gained considerable research attention. Doping with heteroatoms makes it possible to increase the specific capacity and improve the electrochemical performance of carbonaceous materials.[1,2] Such carbonaceous materials have demonstrated electrochemical stability, good energy conversion and bio-imaging applications.[3,4] The most used elements to dope carbonaceous materials are sulfur, boron, nitrogen, and phosphorus. Doping with these materials improves electrical conductivity and power.[5,6] Several methods are used to prepare heteroatom-doped carbon materials, such as external doping,[5] direct pyrolysis,[6] and addition of polymers,[7] and commonly used nitrogen-rich precursors.[8] Polyphosphazenes are polymers with an alternation of phosphorous and nitrogen atoms[9,10] with different chemical structures and functionalities and can be used as precursors to prepare carbon materials.[11,12] Doping of porous carbon with nitrogen and phosphorus proved to result in excellent capacitive performance.[13,14] Nitrogen-doped carbon materials exhibit unique electronegativity that induces an efficient distribution of the electronic charge and thus allows the transport of electrons through the carbon. Furthermore, the positive effect of single doping can be amplified by co-doping causing a synergistic effect.[15,16] Reports demonstrated that a phosphorus dopant[17] exhibits higher electron donation capacity than a nitrogen dopant.[18]

P/N doping on porous carbon has been reported to exhibit excellent performance as an electrode for supercapacitors.[19–21] Supercapacitors have attracted remarkable attention as a component for energy storage and a good alternative to batteries and fuel cells.[22,23] They have distinctive properties with an excellent power density, long lifetimes, fast charging and discharging speeds and higher cycle stability.[24–26] Supercapacitors could be grouped in two categories depending on their charge storage mechanisms: electrochemical double layer capacitors (EDLCs) and pseudo-capacitors.[27,28] EDLCs use ion adsorption between electrode–electrolyte interfaces for energy storage whereas pseudo-capacitors store energy by fast and reversible faradaic reactions. Several carbon-based materials are largely used as electrode materials for EDLCs, such as activated carbon, mesoporous carbon,[29] graphene or reduced graphene oxide (rGO) and carbon aerogels.[30,31] These materials have become indispensable electrode materials because of their high surface areas, porous structures, and good electrical conductivity.[32,33] For pseudo-capacitors, the mostly used materials are conductive polymers and transition metal oxides.[28,34] Non-carbon materials

---

[a] *Department of Chemistry, University of Quebec at Montreal, Montreal, QC, H3C3P8, Canada. E-mail: rhili.khaled@courrier.uqam.ca, chergui.siham@courrier.uqam.ca, juan.abrego@inrs.ca, siaj.mohamed@uqam.ca; Tel: +1 514 987000#192*

[b] *Department of Chemistry, Lebanese University, College of Science III, Campus Mont Michel, 1352, Tripoli, Lebanon. E-mail: aldheiby@ul.edu.lb*

† Electronic supplementary information (ESI) available: Illustration of synthetized reduced graphene oxide, SEM images of GO and FGO, elemental content of PN-rGO determined from XPS analysis and specific capacitance curve of rGO at different current densities. See DOI: **https://doi.org/10.1039/d3ma00553d**

were also studied for improving the capacitance of EDLCs, such as MnO_2 nanoparticles. For example, Misture *et al.* reported the role of existing defects in structures of MnO_2 materials in improving their energy storage densities.[35] On the other hand, Gao *et al.* reported the improvement of pseudo-capacitor properties through an ion de-intercalation protocol using vanadium oxides, leading to a maximum of 460 F g^{-1} at 1 A g^{-1} current density.[36] Further studies on enhancement of the pseudo-capacitance of non-carbon materials were also reported by Liu and co-workers. Their studies involved incorporating selective cations such as Zn and Mn ions into cobaltite materials. The effectiveness of ion incorporation depended on the octahedral geometry of the cobaltites.[37] For this purpose, the performance of the energy storage device can be improved by increasing the surface area, and the specific capacity reaches a plateau when the specific surface is high.[38,39]

In this work, we report a method to prepare nitrogen and phosphorus co-doped microporous derived rGO for supercapacitor applications. The rGO material with thermal stability, high electrical conductivity, large surface area and broad electrochemical window[40,41] was used as an electrode in supercapacitors.

We believe that this proposed study will provide an approach that is scalable for the preparation of new materials based on three-dimensional nitrogen and phosphorus co-doped reduced graphene oxide as superior electrode materials for supercapacitors.

2. Experimental methods

2.1. Materials

Graphite powder (mesh size ≤100 μm), *p*-phenylenediamine (*p*-PDA), hexachlorocyclotriphosphazene (HCCP), potassium carbonate (K_2CO_3), concentrated sulfuric acid (H_2SO_4, 98%), potassium permanganate ($KMnO_4$), hydrogen peroxide aqueous solution (H_2O_2, 30%), phosphoric acid (H_3PO_4, 88%), hydrochloric acid (HCl), toluene, acetone, and methanol were used in this study. Deionised (DI) water was produced using a water purification machine (Milli-Q®). Toluene was dried using 4 Å molecular sieves before being used.

2.2. Synthesis of functionalized graphene oxide (FGO) and P,N-doped reduced graphene oxide (PN-rGO)

The detailed synthesis of rGO is shown in the ESI.† FGO was prepared by functionalizing GO with hexachlorocyclotriphosphazene (HCCP) and *p*-phenylenediamine (*p*-PDA). In a typical experiment, 70 mg of graphene oxide was dispersed in anhydrous toluene (10 mL) and sonicated for 30 min at ambient temperature to yield a dark brown suspension. 1.40 g of K_2CO_3 was added to the GO suspension, and then, HCCP (348 mg, 1 mmol) dissolved in toluene was added dropwise to the mixture with continuous stirring. Then, 325 mg (3 mmol) of *p*-PDA dissolved in toluene was slowly added to the mixture. Afterward, the reaction was refluxed and maintained at 60 °C for 48 h. The as-prepared sample was washed and dried under vacuum at 70 °C for 24 h to obtain FGO. Finally, the sample was annealed in a tubular furnace at 850 °C for 2 h at a ramping rate of 5 °C min^{-1} under an argon atmosphere and the corresponding sample was named PN-rGO. The typical synthesis procedure of PN-rGO is illustrated in Scheme 1.

2.3. Characterization methods

X-ray diffraction (XRD) was performed using a diffractometer (Bruker D8 Advance) with Cu-Kα radiation (λ = 1.54182 Å) in an

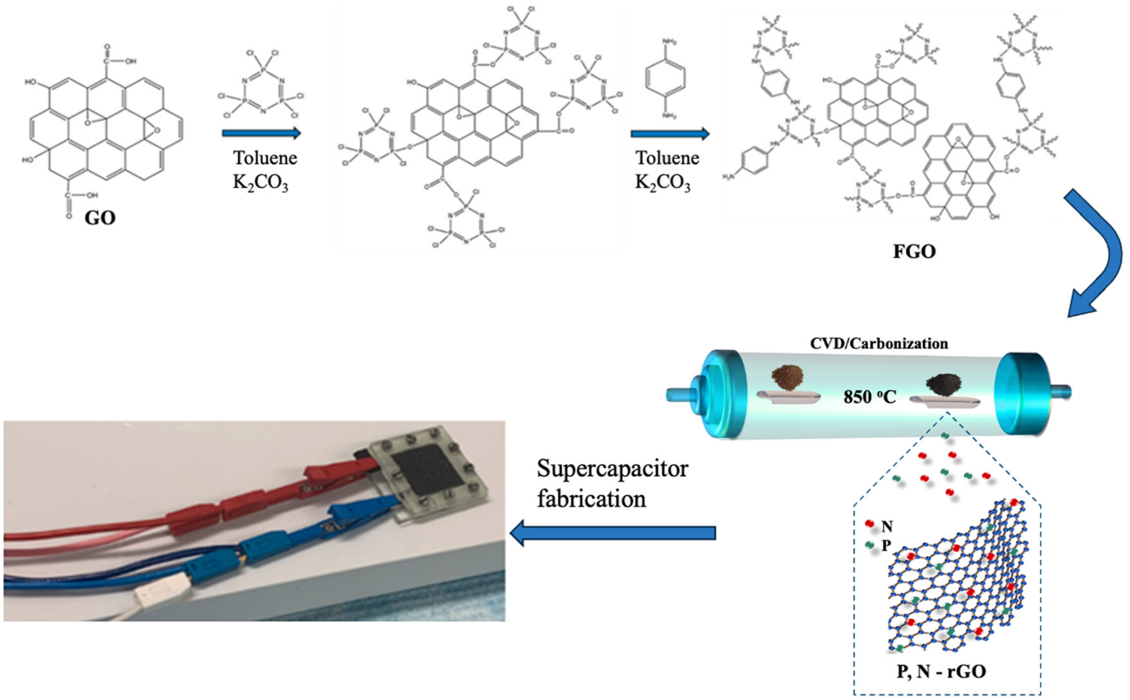

Scheme 1 Schematic illustration of the fabrication process of phosphorus and nitrogen co-doped reduced graphene oxide as superior electrode nanomaterials for the supercapacitor PN-rGO.

angular interval from 20° to 100° at room temperature. The X-ray photoelectron spectroscopy (XPS) data for elemental composition and valence information were collected using a XPS PHI 5600-ci spectrometer (Physical Electronics, Eden Prairie, MN, USA). The morphology of materials was obtained with a scanning electron microscope (SEM) utilizing a JEOL microscope (JSM7600F) operated at 10 kV accelerating voltage and a working distance of 14 mm in secondary electron imaging mode. Transmission electron microscopy (TEM) and energy-dispersive X-ray spectroscopy (EDS) were performed using a Joel JEM-2100F microscope. Raman measurements were acquired using a Renishaw in Via microspectrometer using a 50× objective and a 514 nm laser wavelength.

2.4. Electrochemical tests

The electrochemical performance of the synthesized material was evaluated through cyclic voltammetry (CV), galvanostatic charge/discharge (GCD) and electrochemical impedance spectroscopy (EIS) in a typical three-electrode cell with 6 M KOH aqueous solution as the electrolyte. The working electrode was prepared by mixing the as-prepared materials with 10 μL of Nafion™ solution (5 wt%) and 1 mL of water–ethanol solution with a volume ratio of 4 : 1, and the mixture was then sonicated for 30 min. 18 μL of the resulting ink was drop-casted onto a glassy carbon electrode (GC, A = 0.1256 cm^2) and dried in air at room temperature. An Ag/AgCl electrode and a platinum wire were employed as the reference electrode and counter electrode, respectively. CV curves were obtained at scan rates ranging from 5 to 100 mV s^{-1} with the voltage ranging from −1 V to 0 V. GCD curves were obtained at a current density ranging from 0.5 to 20 A g^{-1}. The EIS measurements were acquired in the frequency range from 100 kHz to 0.01 Hz.

To investigate the potential for practical applications, the performance of the synthesized material was then evaluated in asymmetric supercapacitors through CV, GDC and EIS. The supercapacitor device, as shown in Fig. 7a, consisted of PN-rGO as both the positive and negative electrode materials. Toray (TGP-H-060) carbon paper sections (2 × 2 cm) served as current collectors. Whatman 41 paper was used as the separator and was immersed in the 6 M KOH electrolyte prior to assembly. A Silastic®ERTV Silicone Rubber element was added as the gasket, and the set was sandwiched between two PMMA plates fabricated by computer numerical control (CNC) micromachining. The total mass loading of PN-rGO of positive and negative electrodes was 2 mg. All electrochemical experiments were performed using a Biologic SP-300 potentiate/galvanostatic controlled using EC-Lab software.

The specific capacitance (F g^{-1}) was determined from GCD curves according to eqn (1)

$$C = \frac{I \times \Delta t}{m \times \Delta V} \tag{1}$$

where 'I' is the charge–discharge current (A), Δt is the discharge time (s), ΔV is the potential window (V), and m is the active material loading in the working electrode (g).

The energy (E, W h kg^{-1}) and power (P, W kg^{-1}) densities were calculated from the charge–discharge measurement using eqn (2) and (3), respectively.

$$E = \frac{1}{2}C(\Delta V)^2 \tag{2}$$

where 'C' is the specific capacitance and 'ΔV' is the voltage window of the assembled device.

$$P = \frac{E}{\Delta t} \tag{3}$$

where 'Δt' is the discharge time.

3. Results and discussion

The mechanism of synthesis PN-rGO is summarized in Scheme 1. In the first step, FGO was synthesized by functionalizing GO with hexachlorocyclotriphosphazene (HCCP) and *p*-phenylenediamine (*p*-PDA). Afterwards, the sample was annealed in a tubular furnace at 850 °C for 2 h at a ramp rate of 5 °C min^{-1} under an argon atmosphere. For comparison, rGO was also prepared by following the same preparation process without the addition of HCCP and (*p*-PDA). The morphologies of the obtained materials were characterized by scanning electron microscopy (SEM) and transmission electron microscopy (TEM), as shown in Fig. 1a, b and Fig. S1 (ESI†). From Fig. S1a (ESI†), it can be observed that the GO sheets are almost transparent with some wrinkled structures. Compared to GO, the surface of FGO (Fig. S1b, ESI†) appears to be rough, which indicates that functionalization has been achieved. Fig. 1a indicates the SEM image of rGO, which exhibits wrinkled sheets and random aggregation to a certain degree that led to the formation of well-developed mesopores.[42,43] As can be seen in Fig. 1b, ultrathin, PN-rGO nanosheets showed a partially aggregated and crumpled structure, originating from the defective sites created after the incorporation of nitrogen and phosphorus atoms into the graphene layer. With a higher magnification, as displayed in Fig. 1c, the TEM image shows that the rGO nanosheets are almost transparent with some wrinkles on the surface and have no structural defects. However, the TEM image of PN-rGO (Fig. 1d) shows a mesoporous structure, rough and clearly covered by nanoparticles distributed on the rGO. Elementary mapping (Fig. 1e) was performed to reveal the homogeneous distribution of atoms on the surface: carbon (red), phosphorus (purple), nitrogen (yellow), and (green) oxygen. In addition, the presence of N and P atoms on the PN-rGO is confirmed by signals in the EDX spectrum (Fig. 1f).

XPS was used to investigate the elemental composition and chemical components of the PN-rGO material. As shown in Fig. 2a, the survey XPS spectrum of PN-rGO presents four peaks according to C 1s (285 eV), N 1s (400 eV), O 1s (533 eV) and P 2p (133 eV), proving the successful P, N co-doping in graphene lattices.[44–46] According to the XPS results, the doping amounts of N and P are 2.3% and 4.5%, respectively (Table S1, ESI†). Heteroatoms can improve the wettability of carbon materials, thereby significantly increasing the electrolyte-accessible active surface area and enhancing the specific capacitive performance

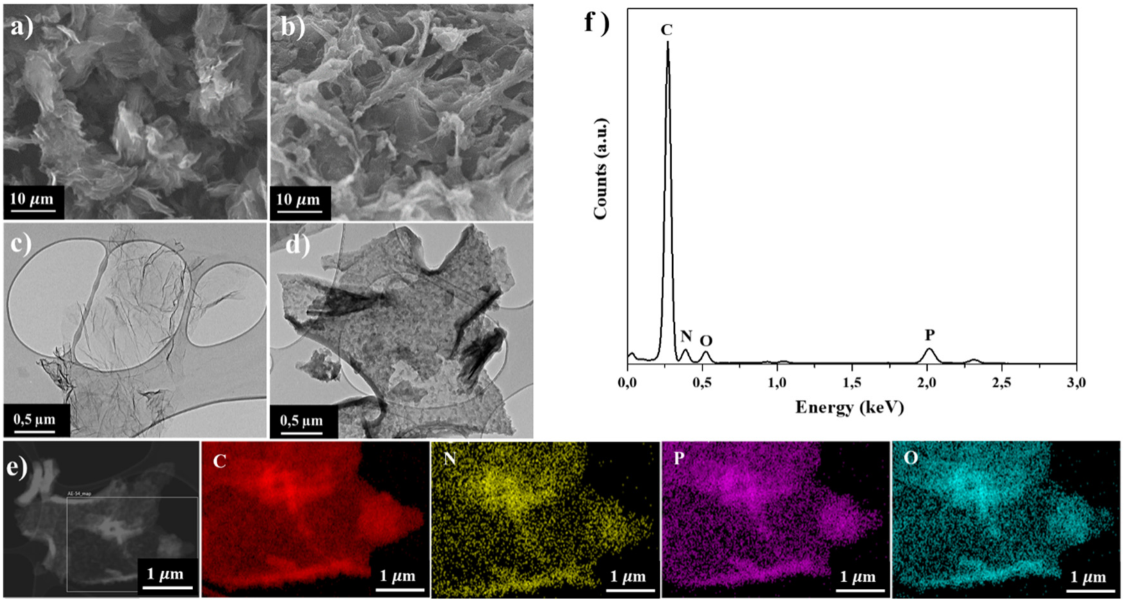

Fig. 1 SEM images of (a) rGO and (b) PN-rGO. TEM images of (c) rGO and (d) PN-rGO. (e) Elemental mapping images of C, P, N, and O components. (f) TEM-EDX spectrum of PN-rGO.

of EDLCs.[47,48] The presence of oxygen in PN-rGO is attributed to the remaining oxygen functional groups.[49] Fig. 2b shows the C 1s spectra of PN-rGO, which can be deconvoluted into four peaks located at about 284.7, 285.4, 286.6, and 289.1 eV, corresponding

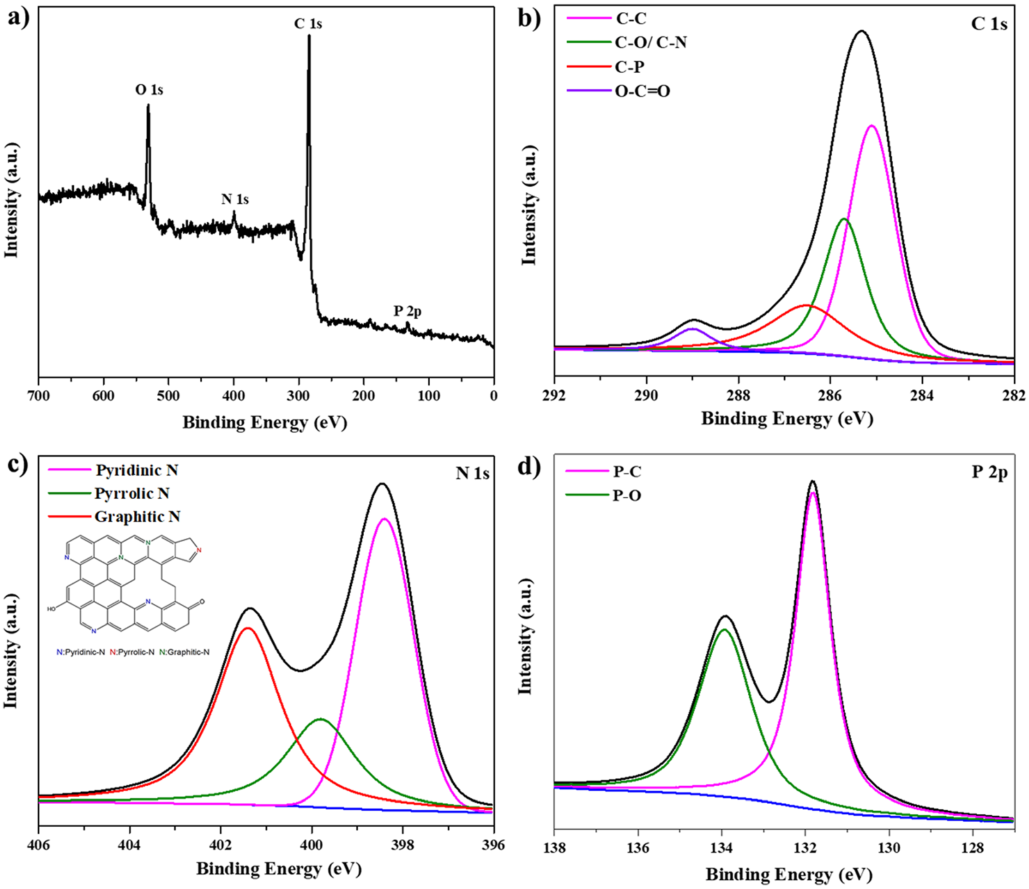

Fig. 2 (a) XPS survey spectra of PN-rGO. High-resolution XPS spectra of the deconvoluted peaks of PN-rGO: (b) C 1s, (c) N 1s, and (d) P 2p spectra of PN-rGO.

to C–C, C–O/C–N, C–P and O–C=O, respectively.[21,50,51] The N 1s spectrum (Fig. 2c) is fitted to three main peaks situated at 398.4 eV, 401.3 eV and 399.7 eV, corresponding to pyridinic-N, graphitic-N, and pyrrolic-N species, respectively.[52,53] The pyridine-N and pyrrolic-N can significantly modify the electronic structure of the material and create active sites to improve the energy density of the supercapacitor.[53,54] Furthermore, graphitic-N is beneficial in improving the electrical conductivity of carbon to reduce the resistance to charge transfer (R_{ct}) during the charge/discharge process.[55] Meanwhile, the P 2p spectrum (Fig. 2d) is deconvoluted into two component peaks at 131.8 and 133.9 eV which correspond to P–C binding and P–O binding, respectively.[56] P has a higher electron donating ability than N, which can greatly improve the charge storage and transport capabilities of carbon materials.[57]

Raman spectroscopy was used to investigate the quality of the carbon nanomaterials of GO, PN-rGO and rGO. As shown in Fig. 3a, two distinct peaks appeared at about 1350 cm^{-1} and 1600 cm^{-1}, corresponding to the D band and G band, respectively.[58] The D band is related to the disordered carbon atoms or the defects in the structure,[59] while the G band is associated with the ordered graphitic structure, and it is originating from the stretching vibrations of sp^2 carbon atoms.[60] Moreover, the intensity ratio value (I_D/I_G) leads to the defect degree of the materials. The I_D/I_G peak intensity ratios of GO, PN-rGO and rGO are 0.83, 0.89, and 0.84, respectively, which means that PN-rGO has more defects compared with GO and rGO due to the incorporated phosphorus and nitrogen atoms in the graphitic plane.[61] The X-ray diffraction (XRD) pattern was used to study the structure information and crystal phase of the samples. Fig. 3b shows the XRD patterns of GO, PN-rGO and rGO. The XRD spectrum of GO exhibits a sharp diffraction peak at 2θ = 10.1° with an interlayer distance of 0.8 nm, corresponding to the plane (002) due to the formation of oxygen functional groups (hydroxyl, carboxyl, and epoxy).[58,62,63] However, for rGO and PN-rGO, the diffraction peak at 10.1° completely disappeared after annealing, replaced by a broad peak at 2θ = 24° with a *d*-spacing of 0.4 nm, revealing the successful reduction of GO to reduced graphene oxide (rGO).

The Brunauer–Emmett–Teller (BET) surface area and pore structure play important roles in the electroactive materials used in supercapacitors. Fig. 4 shows the nitrogen adsorption–desorption isotherms and the corresponding pore size

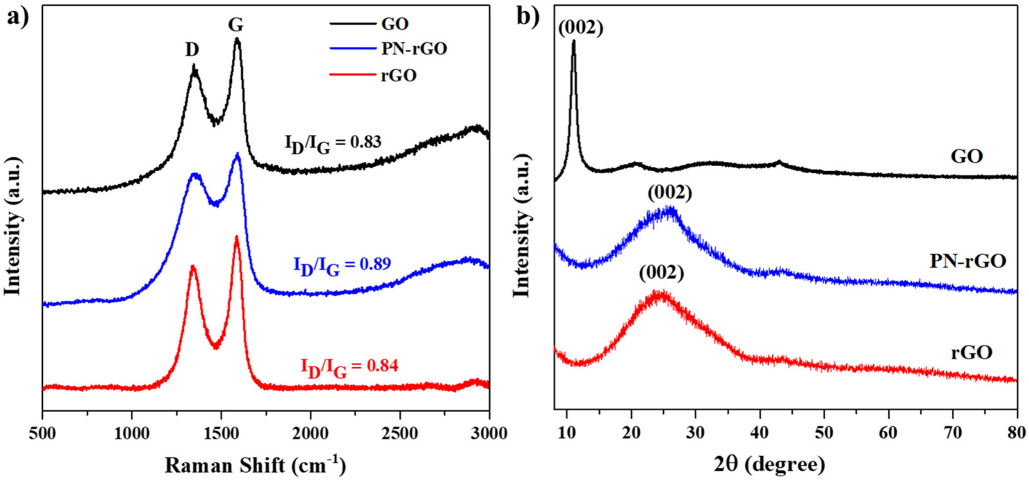

Fig. 3 (a) X-ray diffraction (XRD) patterns and (b) Raman spectra of rGO, PN-rGO and GO.

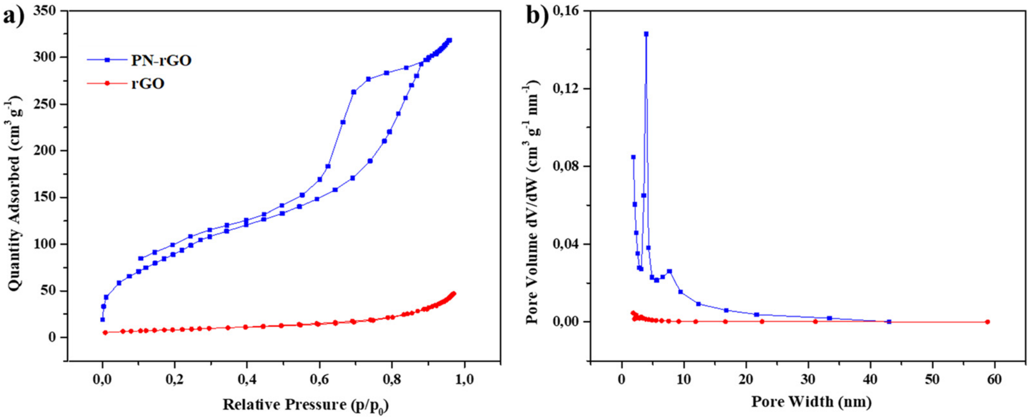

Fig. 4 (a) Nitrogen adsorption–desorption isotherms and (b) corresponding pore size distribution curves of rGO and PN-rGO.

Table 1 BET surface area and pore structure characterization of rGO and PN-rGO

Samples	S_{BET} (m^2 g^{-1})	Pore volume (cm^3 g^{-1})	Average pore size (nm)
rGO	23.7	0.06	2.6
PN-rGO	343.5	0.7	4.5

distribution curves of rGO and PN-rGO samples. The nitrogen adsorption–desorption curves of the PN-rGO sample (Fig. 4a) is type IV (Brunauer–Deming–Deming–Teller (BDDT) classification) with apparent hysteresis loops, indicating the presence of mesopores, which is consistent with the above TEM analysis.[64,65] In contrast, no hysteresis loops are observed on the isotherm curve of rGO, revealing the absence of pores on the GO surface. The BET surface area, pore size and pore volume of rGO and PN-rGO are summarized in Table 1. Based on the BET method, the surface area of PN-rGO is 343.5 m^2 g^{-1}, which is larger than rGO (23.7 m^2 g^{-1}). This is because the gases released from the decomposition of HCCP and *p*-PDA expand graphene sheets, while rGO suffers from restacking, in accordance with the SEM and TEM images.[66] Fig. 4b also shows the pore size distributions of the samples based on the Barret–Joyner–Halenda (BJH) method. The PN-rGO sample exhibits sharp peaks ranging from 2 to 10 nm, suggesting the existence of dominant mesopores. The high surface area and large pore volume of PN-rGO can facilitate the transport of electrolyte ions and enhance energy-storage capacity.[67]

To investigate the electrochemical supercapacitor performance of the as-synthesized materials PN-rGO and rGO, cyclic voltammetry (CV) and galvanostatic charge/discharge (GCD) measurements were evaluated using a three-electrode system with a 6 M KOH electrolyte. Fig. 5a shows the CV curves of PN-rGO and rGO at a scan rate of 50 mV s^{-1} within a potential window of −1 V to 0 V. It can be observed that the CV curves of the two samples are quasi-rectangular, which are typical for electrochemical double-layer capacitors (EDLCs).[68] It is clear that the CV curve area of PN-rGO is the biggest, suggesting that P, N co-doping modification can effectively increase the specific surface area and thus improve the specific capacitance of PN-rGO.[69,70] Fig. 5b displays the GCD curves of PN-rGO and rGO measured at a current density 0.5 A g^{-1}. The curves exhibit a quasi-triangular shape, indicating good electrochemical reversibility.[71] Moreover, the longest charging/discharging time is clearly obtained for PN-rGO compared to rGO, implying higher capacitance, which agrees with the CV results.

The CV measurements of PN-rGO at different scan rates from 5 to 100 mV s^{-1} are revealed in Fig. 6a. As the scan rate increases from 5 to 100 mV s^{-1}, the CV curves still remain a quasi-rectangular shape, indicating ideal capacitive properties.[65,72,73] Additionally, the GCD curves of PN-rGO show a highly symmetrical triangular shape at current densities from 0.5 to 20 A g^{-1} (Fig. 6b), which implied that the material shows good charge/discharge reversibility and cycle performance.[74] The specific capacitance was calculated at different current densities from the GCD curves according to eqn (1). The specific capacitance of PN-rGO (Fig. 6c) was significantly larger than that of rGO (Fig. S2, ESI†) at all measured current densities (0.5 to 20 A g^{-1}). In addition, the capacitance retention of PN-rGO was 70% in the range of 0.5 to 20 A g^{-1}, which indicates good rate capability.[75] The specific capacitance values obtained for PN-rGO (292 F g^{-1} at 0.5 A g^{-1}) supersedes those reported in the literature, which ranged between 178 and 227 F g^{-1}.[76] Moreover, the cycling stability of PN-rGO was investigated through 10 000 charge/discharge cycles at a current density of 10 A g^{-1} (Fig. 6d). The retention ratio of the capacitance value was 97% after 10 000 cycles, suggesting higher stability and excellent cycle performance. These results confirm the excellent synergistic effect of heteroatom doping in the graphene nanosheets.

Electrochemical impedance spectroscopy (EIS) provides information on the accessibility of electrolyte ions through materials. The measured real part of the resistance (Z') is the ohmic resistance originating from the electrolyte and the contact between the electrode and the current collector. Fig. 7 shows the Nyquist plots of the obtained electrode materials. Theoretically, the Nyquist plot consists of two parts: at low frequencies, the straight line is related to the Warburg resistance (Z_W), which indicates the ability of ions to diffuse from the electrolyte to the electrodes, and the nearly vertical slash in the low-frequency region shows the electrical double-layer capacitive behavior.[77–79]

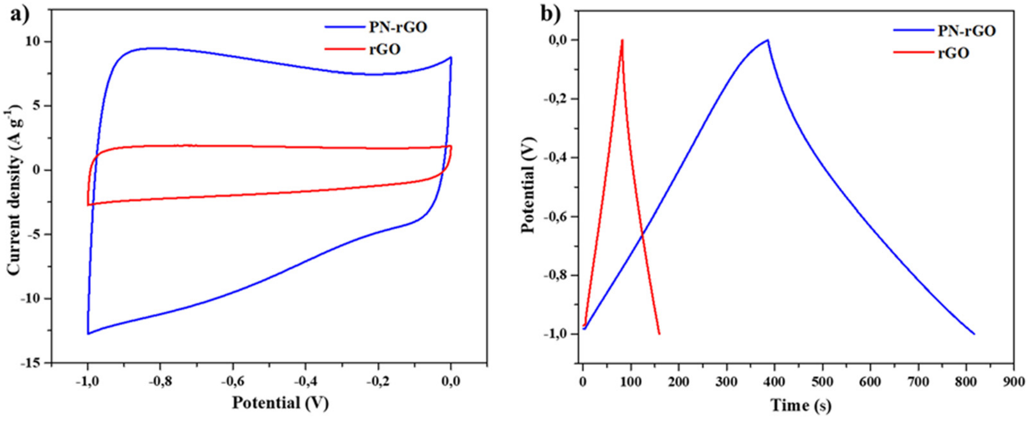

Fig. 5 (a) CV curves of rGO and PN-rGO samples at 50 mV s^{-1}. (b) GCD curves of rGO and PN-rGO at 0.5 A g^{-1}.

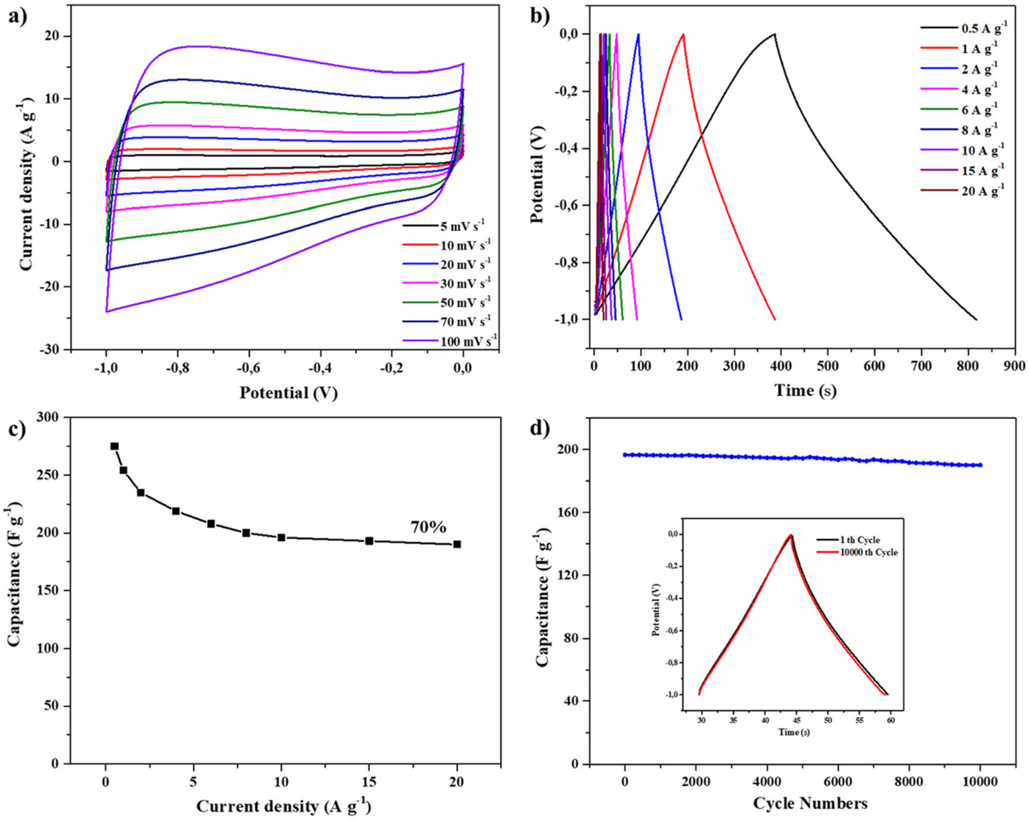

Fig. 6 (a) CV curves of the PN-rGO electrode in the 6 M KOH aqueous solution at different scan rates. (b) GCD curves of the PN-rGO electrode at different current densities. (c) A plot of the specific capacitances calculated from the discharge curves *versus* current density. (d) Cycling stability of the PN-rGO at a current density of 10 A g^{-1}, and the inset shows the first and last cycles of GCD curves.

According to the Nyquist plots (Fig. 7), two regions can be clearly observed, including a semicircle in the high frequency region and a vertical-like slope in the low-frequency region. In the high-frequency region, the semicircle corresponds to the charge-transfer resistance (R_{ct}) at the electrode/electrolyte interface, and a smaller semicircle corresponding to lower charge transfer resistance.[80] The horizontal axis intercept of the Nyquist plot represents the equivalent series resistance (R_S) which can be composed of the intrinsic resistance within the electrolyte, resistance between the interface of the electrode and the electrolyte and contact resistance between the electrode and the current collector.[81] The values of R_S are 2.1 Ω for PN-rGO and 5.6 Ω for rGO. PN-rGO possesses the smallest R_S, indicating that the electrodes have a good contact with the electrolyte.[82] Obviously, PN-rGO has a small semicircle, indicating a small resistance to charge transfer, which is consequently related to its high electrical conductivity.

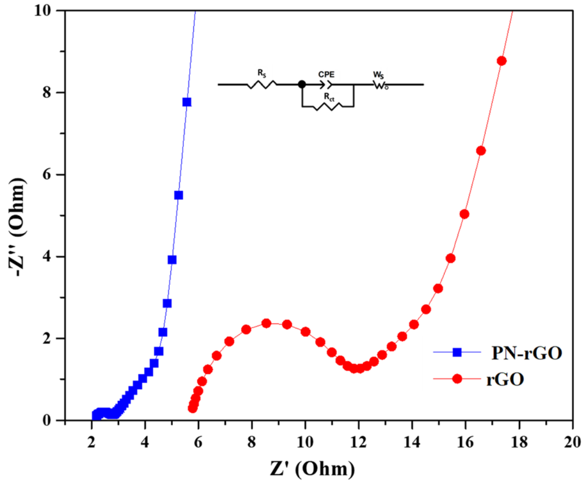

Fig. 7 Nyquist plots of PN-rGO over the frequency range from 0.01 Hz to 100 kHz.

To investigate the potential for practical applications of the PN-rGO based electrodes, a symmetric supercapacitor device was assembled and tested in 6 M KOH aqueous solution in a potential range of 0 to 0.6 V. The electrochemical performance of the device based on two PN-rGO pieces, as positive and negative electrodes, was measured using CV and GCD. The performance of the device was evaluated from the obtained specific capacitance, energy density and power density, as shown in Fig. 8. The schematic illustration of the assembled symmetric supercapacitor is shown in Fig. 8a. The CV curves of the symmetric supercapacitor at various scan rates from 10 to 100 mV s^{-1} are presented in Fig. 8b. The area under the CV curve shows an approximately rectangular shape that was sustained even at a high scan rate of 100 mV s^{-1}, suggesting significant EDLC behaviour and ideal capacitive performance. Fig. 8c displays the GCD curves of the symmetric supercapacitor measured at various current densities from 0.5

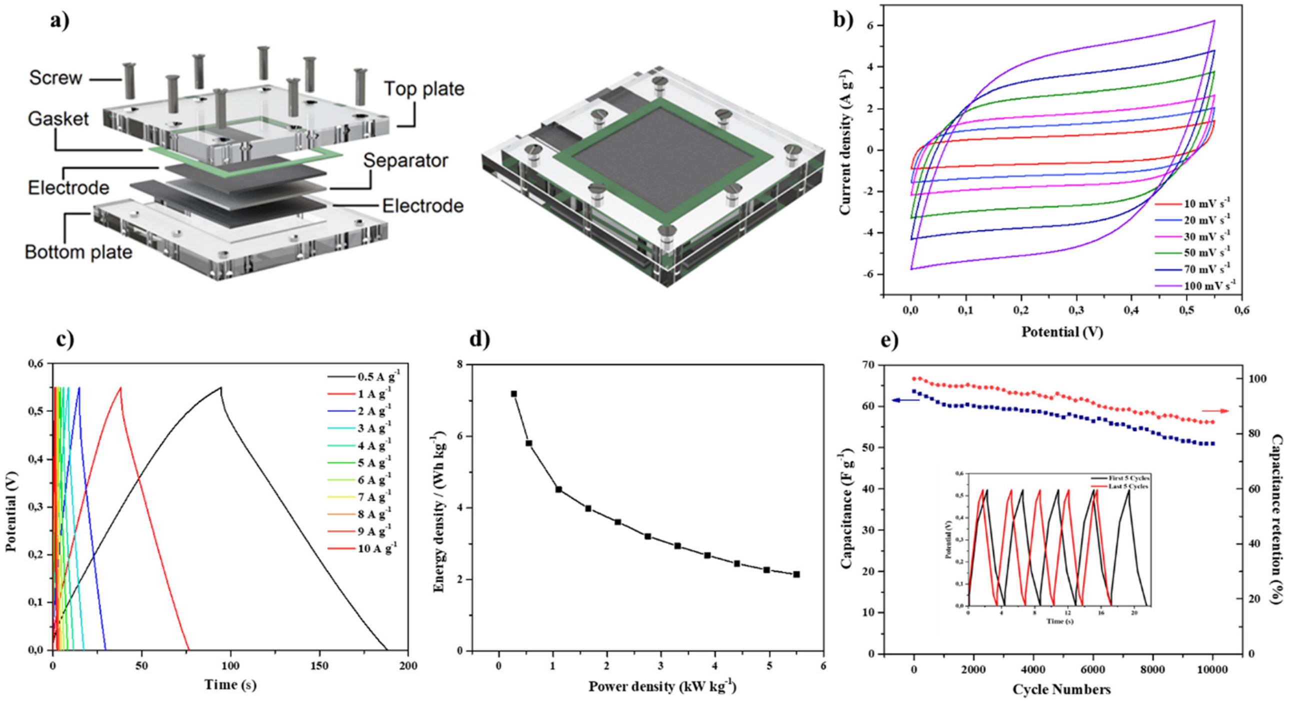

Fig. 8 (a) Schematic illustration of the assembled symmetric supercapacitor. (b) CV curves of the symmetric supercapacitor measured at different scan rates in a potential range of 0–0.6 V in the 6 M KOH electrolyte. (c) GCD curves of the symmetric supercapacitor at different current densities. (d) Ragone plot of the PN-rGO device. (e) Specific capacitance of PN-rGO at various current densities.

to 10 A g^{-1}, exhibiting an almost symmetrical triangle form, which further reveals high reversibility of capacitive behaviour, as consistent with the CV results. Besides, the Ragone plot in Fig. 8d illustrates the performance of the symmetric supercapacitor in terms of power density and energy density and was calculated from the discharge curves using eqn (3) and (4). The NP-rGO device delivered an energy density of 8.2 W h kg^{-1} at a power density of 570 W kg^{-1} at 0.5 A g^{-1}, and retained an energy density of 3.5 W h kg^{-1} at a power density of 6000 W kg^{-1}, which is comparable to those previously reported carbon materials.[83–86] In addition, it has been observed that the symmetrical supercapacitor shows excellent electrochemical stability with 85% retention of the initial capacitance after 10 000 repeated cycles at 6 A g^{-1} (Fig. 8e).

4. Conclusions

In summary, we have successfully prepared PN-rGO materials as electrodes for supercapacitors by direct pyrolysis of the functionalized graphene oxide (FGO). PN-rGO exhibits a high specific capacitance of 292 F g^{-1} at 0.5 A g^{-1}, good rate performance (a retention of 70% from 1 to 20 A g^{-1}) and excellent cycling stability (97% retention of the initial specific capacitance after 10 000 consecutive charge–discharge cycles at 20 A g^{-1}). The assembled symmetric supercapacitor exhibits an energy density of 8.2 W h kg^{-1} at a power density of 570 W kg^{-1}. The incorporation of heteroatoms N and P into carbon materials could effectively modify and improve their electrochemical performance. The current and future work involves further investigation of different cyclomatrix-polyphospazenes with P, N, and S heteroatoms and the study of their respective structures and electrochemical applications.

Conflicts of interest

The authors declare no competing financial interest.

Acknowledgements

This research was funded by the Natural Sciences and Engineering Research Council of Canada (NSERC) and the Canada Research Chairs program (CRC). We thank the Natural Sciences and Engineering Research Council of Canada (NSERC), the Canada Research Chairs program (CRC) and the Canada Foundation for Innovation (CFI). The NanoQAM center at UQAM is gratefully acknowledged for all the characterization experiments. We thank Quebec Centre for Advanced Materials (QCAM).

References

1 J. Wang, C. Wang, S. Gong and Q. Chen, *ACS Appl. Mater. Interfaces*, 2019, **11**, 21567–21577.
2 W. Raza, F. Ali, N. Raza, Y. Luo, K.-H. Kim, J. Yang, S. Kumar, A. Mehmood and E. E. Kwon, *Nano Energy*, 2018, **52**, 441–473.
3 Y. He, X. Han, Y. Du, B. Song, P. Xu and B. Zhang, *ACS Appl. Mater. Interfaces*, 2016, **8**, 3601–3608.
4 Z. Xiang, D. Cao, L. Huang, J. Shui, M. Wang and L. Dai, *Adv. Mater.*, 2014, **26**, 3315–3320.

5 Y. Wang, Y. Li, S. S. Mao, D. Ye, W. Liu, R. Guo, Z. Feng, J. Kong and J. Xie, *Sustainable Energy Fuels*, 2019, **3**, 717–722.

6 G. Ren, Y. Li, Q. Chen, Y. Qian, J. Zheng, Y. Zhu and C. Teng, *ACS Sustainable Chem. Eng.*, 2018, **6**, 16032–16038.

7 L. Hu, Q. Zhu, Q. Wu, D. Li, Z. An and B. Xu, *ACS Sustainable Chem. Eng.*, 2018, **6**, 13949–13959.

8 Y. Song, J. Yang, K. Wang, S. Haller, Y. Wang, C. Wang and Y. Xia, *Carbon*, 2016, **96**, 955–964.

9 K. Chen, X. Huang, C. Wan and H. Liu, *Electrochim. Acta*, 2016, **222**, 543–550.

10 H. R. Allcock, *J. Inorg. Organomet. Polym. Mater.*, 2006, **16**, 277–294.

11 S. Zhang, S. Ali, H. Ma, L. Zhang, Z. Wu, D. Wu and T. S. Hu, *J. Phys. Chem. B*, 2016, **120**, 11307–11316.

12 H. R. Allcock, *Dalton Trans.*, 2016, **45**, 1856–1862.

13 X. Zhang, J. Zhao, X. He, Q. Li, C. Ao, T. Xia, W. Zhang, C. Lu and Y. Deng, *Carbon*, 2018, **127**, 236–244.

14 H. R. Allcock and N. L. Morozowich, *Polym. Chem.*, 2012, **3**, 578–590.

15 W. Liu, S. Zhang, S. U. Dar, Y. Zhao, R. Akram, X. Zhang, S. Jin, Z. Wu and D. Wu, *Carbon*, 2018, **129**, 420–427.

16 H. R. Allcock, G. S. McDonnell, G. H. Riding and I. Manners, *Chem. Mater.*, 1990, **2**, 425–432.

17 Z. Tian, A. Hess, C. R. Fellin, H. Nulwala and H. R. Allcock, *Macromolecules*, 2015, **48**, 4301–4311.

18 D. Momodu, N. F. Sylla, B. Mutuma, A. Bello, T. Masikhwa, S. Lindberg, A. Matic and N. Manyala, *J. Electroanal. Chem.*, 2019, **838**, 119–128.

19 C. Wang, L. Sun, Y. Zhou, P. Wan, X. Zhang and J. Qiu, *Carbon*, 2013, **59**, 537–546.

20 J. Chen, H. Wei, H. Chen, W. Yao, H. Lin and S. Han, *Electrochim. Acta*, 2018, **271**, 49–57.

21 Y. Ma, D. Wu, T. Wang and D. Jia, *ACS Appl. Energy Mater.*, 2019, **3**, 957–969.

22 A. Berrueta, A. Ursúa, I. San Martín, A. Eftekhari and P. Sanchis, *IEEE Access*, 2019, **7**, 50869–50896.

23 M. D. Stoller and R. S. Ruoff, *Energy Environ. Sci.*, 2010, **3**, 1294–1301.

24 M. Zhou, A. Vassallo and J. Wu, *ACS Appl. Energy Mater.*, 2020, **3**, 5993–6000.

25 Y. Shao, M. F. El-Kady, J. Sun, Y. Li, Q. Zhang, M. Zhu, H. Wang, B. Dunn and R. B. Kaner, *Chem. Rev.*, 2018, **118**, 9233–9280.

26 J. Li, L. An, H. Li, J. Sun, C. Shuck, X. Wang, Y. Shao, Y. Li, Q. Zhang and H. Wang, *Nano Energy*, 2019, **63**, 103848.

27 W. Chen, R. Rakhi and H. N. Alshareef, *J. Mater. Chem.*, 2012, **22**, 14394–14402.

28 Y. Zhang, H. Feng, X. Wu, L. Wang, A. Zhang, T. Xia, H. Dong, X. Li and L. Zhang, *Int. J. Hydrogen Energy*, 2009, **34**, 4889–4899.

29 M. Sevilla and R. Mokaya, *Energy Environ. Sci.*, 2014, **7**, 1250–1280.

30 M. Inagaki, H. Konno and O. Tanaike, *J. Power Sources*, 2010, **195**, 7880–7903.

31 A. G. Pandolfo and A. F. Hollenkamp, *J. Power Sources*, 2006, **157**, 11–27.

32 O. Sadak, A. K. Sundramoorthy and S. Gunasekaran, *Carbon*, 2018, **138**, 108–117.

33 N. Guo, M. Li, Y. Wang, X. Sun, F. Wang and R. Yang, *ACS Appl. Mater. Interfaces*, 2016, **8**, 33626–33634.

34 G. M. Jacob, Q. M. Yang and I. Zhitomirsky, *J. Appl. Electrochem.*, 2009, **39**, 2579–2585.

35 P. Gao, P. Metz, T. Hey, Y. Gong, D. Liu, D. D. Edwards, J. Y. Howe, R. Huang and S. T. Misture, *Nat. Commun.*, 2017, **8**, 14559.

36 Y. Zeng, J. Hu, J. Yang, P. Tang, Q. Fu, W. Zhou, Y. Peng, P. Xiao, S. Chen and K. Guo, *J. Mater. Chem. A*, 2022, **10**, 10439–10451.

37 P. Tang, P. Gao, X. Cui, Z. Chen, Q. Fu, Z. Wang, Y. Mo, H. Liu, C. Xu and J. Liu, *Adv. Energy Mater.*, 2022, **12**, 2102053.

38 J. Xia, F. Chen, J. Li and N. Tao, *Nat. Nanotechnol.*, 2009, **4**, 505–509.

39 J. Zhang, L. Gong, K. Sun, J. Jiang and X. Zhang, *J. Solid State Electrochem.*, 2012, **16**, 2179–2186.

40 A. K. Geim and K. S. Novoselov, *Nat. Mater.*, 2007, **6**, 183–191.

41 C. Liu, Z. Yu, D. Neff, A. Zhamu and B. Z. Jang, *Nano Lett.*, 2010, **10**, 4863–4868.

42 X. Wang, Y. Hu, J. Min, S. Li, X. Deng, S. Yuan and X. Zuo, *Appl. Sci.*, 2018, **8**, 1950.

43 Z. Liu, H. Zhou, Z. Huang, W. Wang, F. Zeng and Y. Kuang, *J. Mater. Chem. A*, 2013, **1**, 3454–3462.

44 S. Yang, L. Zhi, K. Tang, X. Feng, J. Maier and K. Müllen, *Adv. Funct. Mater.*, 2012, **22**, 3634–3640.

45 D.-S. Yang, D. Bhattacharjya, S. Inamdar, J. Park and J.-S. Yu, *J. Am. Chem. Soc.*, 2012, **134**, 16127–16130.

46 K. Rhili, S. Chergui, A. Samih ElDouhaibi, A. Mazzah and M. Siaj, *ACS Omega*, 2023, **8**, 9137–9144.

47 J. Hou, K. Jiang, R. Wei, M. Tahir, X. Wu, M. Shen, X. Wang and C. Cao, *ACS Appl. Mater. Interfaces*, 2017, **9**, 30626–30634.

48 M. Salanne, B. Rotenberg, K. Naoi, K. Kaneko, P.-L. Taberna, C. P. Grey, B. Dunn and P. Simon, *Nat. Energy*, 2016, **1**, 1–10.

49 D. Wei, Y. Liu, Y. Wang, H. Zhang, L. Huang and G. Yu, *Nano Lett.*, 2009, **9**, 1752–1758.

50 J. Zhang, J. Jiang and X. Zhao, *J. Phys. Chem. C*, 2011, **115**, 6448–6454.

51 X. Li, Z. Lv, M. Wu, X. Li and Z. Li, *J. Electroanal. Chem.*, 2021, **881**, 114952.

52 L. Lai, J. R. Potts, D. Zhan, L. Wang, C. K. Poh, C. Tang, H. Gong, Z. Shen, J. Lin and R. S. Ruoff, *Energy Environ. Sci.*, 2012, **5**, 7936–7942.

53 A. Ananthanarayanan, Y. Wang, P. Routh, M. A. Sk, A. Than, M. Lin, J. Zhang, J. Chen, H. Sun and P. Chen, *Nanoscale*, 2015, **7**, 8159–8165.

54 Z. Li, Y. Wang, W. Xia, J. Gong, S. Jia and J. Zhang, *Nanomaterials*, 2020, **10**, 1912.

55 D. Hulicova-Jurcakova, M. Seredych, G. Q. Lu and T. J. Bandosz, *Adv. Funct. Mater.*, 2009, **19**, 438–447.

56 B. Li, F. Dai, Q. Xiao, L. Yang, J. Shen, C. Zhang and M. Cai, *Energy Environ. Sci.*, 2016, **9**, 102–106.

57 J. Yi, Y. Qing, C. Wu, Y. Zeng, Y. Wu, X. Lu and Y. Tong, *J. Power Sources*, 2017, **351**, 130–137.

58 K. Rhili, S. Chergui, A. S. ElDouhaibi and M. Siaj, *ACS Omega*, 2021, **6**, 6252–6260.

59 S. Verma and R. K. Dutta, *RSC Adv.*, 2015, **5**, 77192–77203.

60 M. Pimenta, G. Dresselhaus, M. S. Dresselhaus, L. Cancado, A. Jorio and R. Saito, *Phys. Chem. Chem. Phys.*, 2007, **9**, 1276–1290.

61 M. Gao, J. Fu, M. Wang, K. Wang, S. Wang, Z. Wang, Z. Chen and Q. Xu, *J. Colloid Interface Sci.*, 2018, **524**, 165–176.

62 A. Kaniyoor, T. T. Baby and S. Ramaprabhu, *J. Mater. Chem.*, 2010, **20**, 8467–8469.

63 W. Hu, J. Zhan, X. Wang, N. Hong, B. Wang, L. Song, A. A. Stec, T. R. Hull, J. Wang and Y. Hu, *Ind. Eng. Chem. Res.*, 2014, **53**, 3073–3083.

64 Y. Zhang, Q. Sun, K. Xia, B. Han, C. Zhou, Q. Gao, H. Wang, S. Pu and J. Wu, *ACS Sustainable Chem. Eng.*, 2019, **7**, 5717–5726.

65 L. Wan, R. Xiao, J. Liu, Y. Zhang, J. Chen, C. Du and M. Xie, *Appl. Surf. Sci.*, 2020, **518**, 146265.

66 S. Gadipelli and Z. X. Guo, *Prog. Mater. Sci.*, 2015, **69**, 1–60.

67 Y. Sun, J. Xue, S. Dong, Y. Zhang, Y. An, B. Ding, T. Zhang, H. Dou and X. Zhang, *J. Mater. Sci.*, 2020, **55**, 5166–5176.

68 Y. Bai, R. Rakhi, W. Chen and H. N. Alshareef, *J. Power Sources*, 2013, **233**, 313–319.

69 H. Cheng, F. Yi, A. Gao, H. Liang, D. Shu, X. Zhou, C. He and Z. Zhu, *ACS Appl. Energy Mater.*, 2019, **2**, 4084–4091.

70 J. Li, X. Yun, Z. Hu, L. Xi, N. Li, H. Tang, P. Lu and Y. Zhu, *J. Mater. Chem. A*, 2019, **7**, 26311–26325.

71 Y. Liu, Z. Chang, L. Yao, S. Yan, J. Lin, J. Chen, J. Lian, H. Lin and S. Han, *J. Electroanal. Chem.*, 2019, **847**, 113111.

72 F. Qi, Z. Xia, W. Wei, H. Sun, S. Wang and G. Sun, *Electrochim. Acta*, 2017, **246**, 59–67.

73 E. Lei, W. Li, C. Ma, Z. Xu and S. Liu, *Appl. Surf. Sci.*, 2018, **457**, 477–486.

74 L. Zheng, B. Tang, X. Dai, T. Xing, Y. Ouyang, Y. Wang, B. Chang, H. Shu and X. Wang, *Chem. Eng. J.*, 2020, **399**, 125671.

75 Z.-G. Yang, N.-N. Liu, S. Dong, F.-S. Tian, Y.-P. Gao and Z.-Q. Hou, *SN Appl. Sci.*, 2019, **1**, 1–9.

76 Z. Lin, Y. Liu, Y. Yao, O. J. Hildreth, Z. Li, K. Moon and C.-P. Wong, *J. Phys. Chem. C*, 2011, **115**, 7120–7125.

77 D. Antiohos, K. Pingmuang, M. S. Romano, S. Beirne, T. Romeo, P. Aitchison, A. Minett, G. Wallace, S. Phanichphant and J. Chen, *Electrochim. Acta*, 2013, **101**, 99–108.

78 Y. Bu, T. Sun, Y. Cai, L. Du, O. Zhuo, L. Yang, Q. Wu, X. Wang and Z. Hu, *Adv. Mater.*, 2017, **29**, 1700470.

79 A. Eftekhari, *J. Mater. Chem. A*, 2018, **6**, 2866–2876.

80 F. Xu, R. Cai, Q. Zeng, C. Zou, D. Wu, F. Li, X. Lu, Y. Liang and R. Fu, *J. Mater. Chem.*, 2011, **21**, 1970–1976.

81 L. Miao, D. Zhu, M. Liu, H. Duan, Z. Wang, Y. Lv, W. Xiong, Q. Zhu, L. Li and X. Chai, *Chem. Eng. J.*, 2018, **347**, 233–242.

82 T. Kim, G. Jung, S. Yoo, K. S. Suh and R. S. Ruoff, *ACS Nano*, 2013, **7**, 6899–6905.

83 Z. Shen, Y. Mo, J. Du and A. Chen, *Appl. Surf. Sci.*, 2020, **527**, 146845.

84 X. Chen, K. Wu, B. Gao, Q. Xiao, J. Kong, Q. Xiong, X. Peng, X. Zhang and J. Fu, *Waste Biomass Valorization*, 2016, **7**, 551–557.

85 D. Xue, D. Zhu, W. Xiong, T. Cao, Z. Wang, Y. Lv, L. Li, M. Liu and L. Gan, *ACS Sustainable Chem. Eng.*, 2019, **7**, 7024–7034.

86 K. Xia, Z. Huang, L. Zheng, B. Han, Q. Gao, C. Zhou, H. Wang and J. Wu, *J. Power Sources*, 2017, **365**, 380–388.